The Astrophysical Journal, 797:111 (8pp), 2014 December 20 doi:10.1088/0004-637X/797/2/111

NuSTAR OBSERVATIONS AND BROADBAND SPECTRAL ENERGY DISTRIBUTION MODELING OF THE MILLISECOND PULSAR BINARY PSR J1023+0038

K. L. Li[1], A. K. H. Kong[1], J. Takata[2], K. S. Cheng[2], P. H. T. Tam[1], C. Y. Hui[3], and Ruolan Jin[1]
[1] Institute of Astronomy and Department of Physics, National Tsing Hua University, Hsinchu 30013, Taiwan; liliraykh@gmail.com, akong@phys.nthu.edu.tw
[2] Department of Physics, University of Hong Kong, Pokfulam Road, Hong Kong; takata@hku.hk
[3] Department of Astronomy and Space Science, Chungnam National University, Daejeon, Korea
Received 2014 May 19; accepted 2014 October 16; published 2014 December 5

ABSTRACT

We report the first hard X-ray (3–79 keV) observations of the millisecond pulsar (MSP) binary PSR J1023+0038 using *NuSTAR*. This system has been shown transiting between a low-mass X-ray binary (LMXB) state and a rotation-powered MSP state. The *NuSTAR* observations were taken in both LMXB state and rotation-powered state. The source is clearly seen in both states up to ∼79 keV. During the LMXB state, the 3–79 keV flux is about a factor of 10 higher than in the rotation-powered state. The hard X-rays show clear orbital modulation during the X-ray faint rotation-powered state but the X-ray orbital period is not detected in the X-ray bright LMXB state. In addition, the X-ray spectrum changes from a flat power-law spectrum during the rotation-powered state to a steeper power-law spectrum in the LMXB state. We suggest that the hard X-rays are due to the intrabinary shock from the interaction between the pulsar wind and the injected material from the low-mass companion star. During the rotation-powered MSP state, the X-ray orbital modulation is due to Doppler boosting of the shocked pulsar wind. At the LMXB state, the evaporating matter of the accretion disk due to the gamma-ray irradiation from the pulsar stops almost all the pulsar wind, resulting in the disappearance of the X-ray orbital modulation.

Key words: accretion, accretion disks – binaries: close – pulsars: individual (PSR J1023+0038) – X-rays: binaries

Online-only material: color figures

1. INTRODUCTION

Millisecond pulsars (MSPs) are widely believed to be the descent of low-mass X-ray binaries (LMXBs). Based on current theoretical models, the rotating neutron star in an LMXB can be spun up to millisecond periods via accretion from the low-mass companion that transfers mass and angular momentum to the pulsar (e.g., Alpar et al. 1982). The first evidence of this "recycling" scenario comes from the discovery of accreting millisecond X-ray pulsars in LMXBs (e.g., Wijnands & van der Klis 1998). When the accretion stops and the accretion disk is removed, the system will become an MSP powered by rotation. It is still a puzzle how and when this process happens. Possible models include pulsar wind ablation (Wang et al. 2009), propeller effect (Romanova et al. 2009), and gamma-ray heating from the MSP (Takata et al. 2010).

To investigate the evolutionary process of MSPs and LMXBs, one has to look for a system that shows both rotation-powered MSP and LMXB behaviors. The discovery of the MSP/X-ray binary PSR J1023+0038 (hereafter J1023) is key to understanding the state transition between an LMXB and an MSP. J1023 was first suggested as a magnetic cataclysmic variable (Bond et al. 2002) and was subsequently identified as an LMXB candidate (Thorstensen & Armstrong 2005; Homer et al. 2006). Radio observations then show that J1023 is a 1.69 ms pulsar in a 4.8 hr binary orbit with a $\sim 0.2\ M_{\odot}$ companion star (Archibald et al. 2009), establishing a link between an MSP and an LMXB. Interestingly, the system clearly shows the accretion disk signature before 2002 (Wang et al. 2009), but the disk has disappeared since then. This is direct evidence of a state transition from an LMXB to an MSP. More recently, the X-ray emission of J1023 has increased by a factor of about 20 (Kong 2013; Patruno et al. 2014; Takata et al. 2014) since 2013 October and the radio pulsation has disappeared after 2013 mid-June (Stappers et al. 2014). Meanwhile, the UV emission has brightened by four magnitudes (Patruno et al. 2014), and the accretion disk has reemerged based on optical spectroscopy (Takata et al. 2014), indicating that J1023 has switched from an MSP to an LMXB. It is now clear that J1023 underwent two state transitions between an LMXB and an MSP. It is worth noting that there are two similar systems, IGR J18245–2452 (Papitto et al. 2013) and XSS J12270–4859 (Bassa et al. 2014), that also show similar state transitions. Such state change events have proven solidly that MSPs are evolved from LMXBs.

J1023 has been observed in X-ray with *Chandra*, *XMM-Newton*, and *Swift* in the past decade. In particular, the *XMM-Newton* observations reveal the X-ray pulsation as well as the X-ray orbital modulation (Archibald et al. 2010; Tam et al. 2010) when the source is in the X-ray faint rotation-powered state. During the recent X-ray bright LMXB state, the X-Ray Telescope (XRT) on board *Swift* detected the soft (0.3–10 keV) X-ray brightening (Kong 2013; Patruno et al. 2014; Takata et al. 2014) while the Burst Alert Telescope (BAT) failed to detect the hard (15–50 keV) X-rays (Stappers et al. 2014). J1023 also has gamma-rays (200 MeV–20 GeV) detectable with the *Fermi Gamma-Ray Space Telescope* in both rotation-powered and LMXB states (Tam et al. 2010; Takata et al. 2014).

In this paper, we report the first *NuSTAR* hard X-ray (3–79 keV) observations of J1023 taken before and after its recent MSP/LMXB state change and discuss the origin of the X-ray emission in the context of an intrabinary shock model.

2. OBSERVATIONS AND DATA REDUCTION

NuSTAR is the first focusing hard XRT that is sensitive to 3–79 keV (Harrison et al. 2013). It observed J1023 four times with the onboard focal plane modules A and B (FPMA/B) in 2013 mid-June and mid-October, during which the MSP was

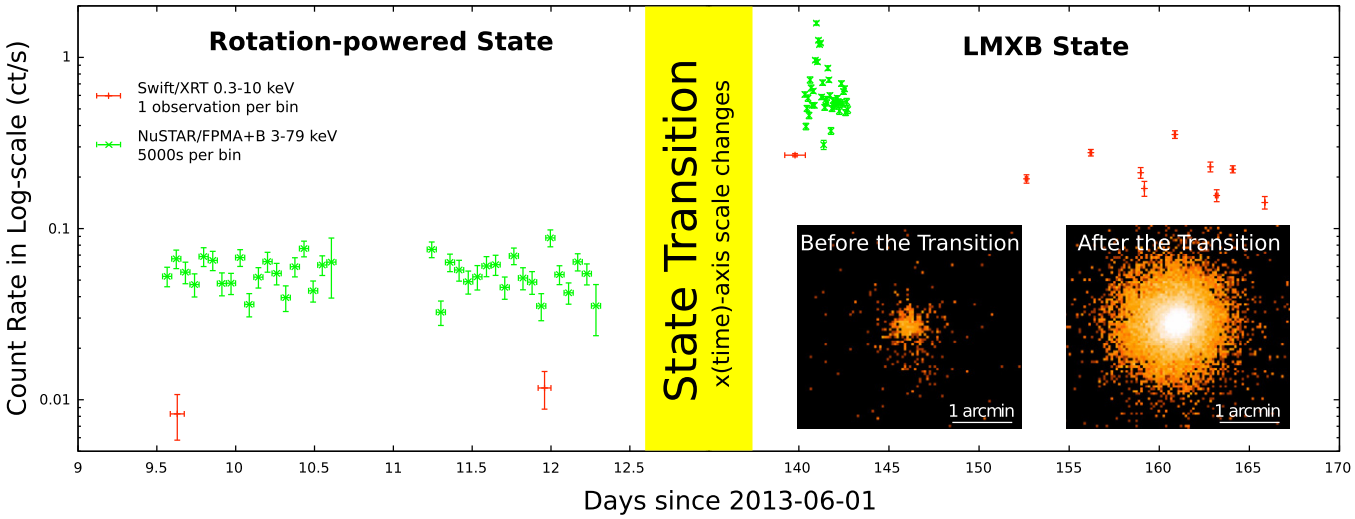

Figure 1. Long-term X-ray light curves of *NuSTAR*/FPMA/B (green) and *Swift*/XRT (red; see Takata et al. 2014 for details) before/after the state transition with different time-axis scales. The inset box shows the *NuSTAR*/FPMA+B images before/after the transition. The intensity ratio between the two images is about 10.
(A color version of this figure is available in the online journal.)

in the rotation-powered (X-ray low state) and LMXB (X-ray high state) states, respectively (Patruno et al. 2014; Takata et al. 2014). Figure 1 shows the long-term light curves of J1023 observed with *NuSTAR* and *Swift* since 2013 June 1. The total exposure time for the first three observations taken in 2013 June is 94.1 ks, which is roughly the same as the last observation in 2013 October with an integration time of 94.3 ks. We downloaded data products of the observations including the housekeeping, auxiliary, and cleaned/calibrated events (i.e., Level 2) files from the HEASARC data archive. The X-ray counterpart of J1023 is clearly detected within the *NuSTAR*'s absolute astrometric accuracy (5″at 90% confidence; Alexander et al. 2013) in all observations, and the source is significantly brighter after the state transition (see the inset box of Figure 1).

Scientific data extractions are performed using the HEASARC's HEASoft multi-mission software (version 6.15.1) together with NuSTARDAS v1.3.1 and the updated *NuSTAR* calibration database (CALDB version 20131223) by following the instructions outlined in the *NuSTAR* Data Analysis Software Guide.[4] The X-ray spectra, the corresponding response matrices, and the light curves used in this work are produced by a *NuSTAR*-specific task nuproducts by keeping most of the parameters of the task default, but using different pulse-invariant channel ranges of interest (which will be discussed in Section 3.2) and turning the barycentric correction option on. For the extraction regions, we choose different sizes of source regions based on the source count rate of the epoch. For the low-state observations, a circular source region of 30″ radius and a source-free annulus background region of 80″/160″ inner/outer radii around the source are applied. For the high-state observation, we used a larger circular source region of 50″ radius to encompass more useful source photons. As the source is close to the contact between the chips (each FPM consists of a 2 × 2 cadmium–zinc–tellurium detector array), we select three circular regions with radii of 50″ (identical to the source region) at similar chip positions as the background to minimize the inconsistency between the source/background samplings. Unless otherwise mentioned, the uncertainties listed in this paper are at a 90% confidence level.

[4] http://heasarc.gsfc.nasa.gov/docs/nustar/analysis/nustardas_swguide_v1.5.pdf

3. DATA ANALYSIS AND RESULTS

3.1. Spectral Analysis

We performed X-ray spectral model fittings for all four data sets with XSPEC. Since the numbers of detected photons are small for the first three observations taken in the X-ray low state, we therefore stacked the three data sets for spectral analysis. As *NuSTAR* observed J1023 roughly simultaneously with *Swift*/XRT (Figure 1), we also included the high-state XRT spectrum to have a much wider energy range (0.3–79 keV) for the spectral fittings, while the low-state XRT spectrum is not used because of its very limited photon statistics. Details of the *Swift*/XRT spectrum/light curve used in this analysis have been discussed in our previous paper (Takata et al. 2014). All spectra were grouped with at least 25 counts per spectral bin to allow χ^2 statistics.

During the quiescence, the spectrum can be fit with an absorbed power-law model (χ^2/dof = 56.24/76; Figure 2) with a column density $N_{\rm H} < 3.4 \times 10^{22}\,{\rm cm}^{-2}$, a photon index of $\Gamma = 1.20^{+0.14}_{-0.09}$, and an observed 3–79 keV flux of $F_{\rm obs} = 2.89^{+0.26}_{-0.5} \times 10^{-12}\,{\rm erg\,cm^{-2}\,s^{-1}}$ (Figure 2), which are consistent with the spectral fitting result of the 83.1 ks *Chandra* observation taken on 2010 March 24 (Bogdanov et al. 2011). The absorption parameter is poorly constrained since the photoelectric absorption is only sensitive to soft X-rays (i.e., less than 2 keV), instead of the hard *NuSTAR*'s energy band. Nonetheless, for the same reason, the ambiguous column density does not significantly affect our result. In fact, the observed and the absorption-corrected fluxes of the fits are almost the same. For the *NuSTAR* and *Swift* observations taken during the LMXB state, an absorbed power law is still the best model yielding a chi-square statistic value of χ^2/dof = 1296.29/985 with the best-fit values of $N_{\rm H} = 4.9^{+0.8}_{-0.7} \times 10^{20}\,{\rm cm}^{-2}$, $\Gamma = 1.63 \pm 0.01$, and $F_{\rm obs} = 2.67^{+0.05}_{-0.04} \times 10^{-11}\,{\rm erg\,cm^{-2}\,s^{-1}}$ (Figure 2). All parameters including the column density are greatly constrained due to a much higher signal-to-noise ratio and a wider energy

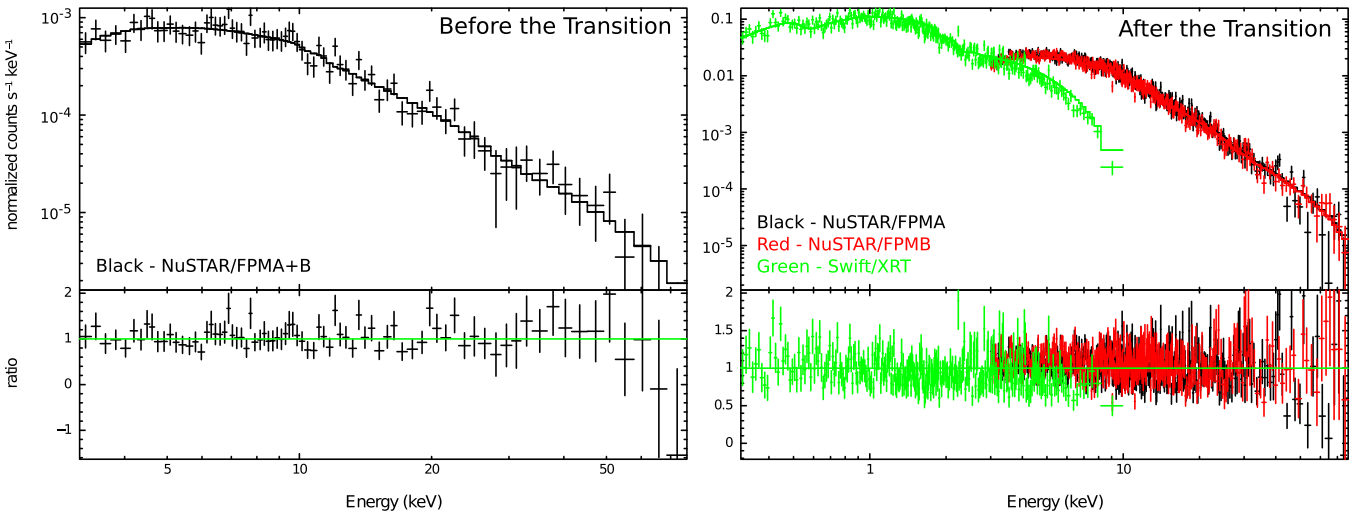

Figure 2. *NuSTAR*/FPMA+B (and *Swift*/XRT) spectra of J1023 during the rotation-powered state (left) and the LMXB state (right). Both data sets can be fit with a simple power law. The X-ray flux during the LMXB state is about 10 higher than the quiescent value, and the photon index is significantly softer.
(A color version of this figure is available in the online journal.)

range (i.e., 0.3–79 keV) of the resultant spectrum. Compared to the quiescent observations, the photon index is significantly softer, and the observed flux is about 10 times larger after the state transition, which is consistent with the previous *Swift*/XRT observations (Patruno et al. 2014; Takata et al. 2014).

Besides a simple power-law model, we tried to add a high-energy exponential cutoff component to improve the spectral fitting results of the *NuSTAR* data. However, based on the χ^2 values, the improvement is insignificant for the high-state spectrum (the *F*-test probability is 59%), and there is no improvement for the low state. Furthermore, the best-fit cutoff energy is about 800 keV for the high state and is pegged to the maximum allowed value (i.e., 5000 keV) for the low state. In addition to the unreasonable large uncertainties of the cutoff energies (i.e., a few times that of the best-fit value), both cutoff energies are significantly larger than the energy range of *NuSTAR* strongly suggesting that the fits are unreliable. Therefore, we conclude that a simple power-law model is the best spectral model for the data.

3.2. Temporal Analysis

To search for the hard X-ray orbital modulation of J1023, we use the `XRONOS` package to analyze the *NuSTAR* low- and high-state light curves that cover about 5.5 orbital cycles. The barycentric correction is applied to the light curves as mentioned in Section 2. We also set the bin size of the light curves to 10 s, which is fine enough to search for the 4.8 hr orbital period (Thorstensen & Armstrong 2005; Archibald et al. 2009). Since the source light curves generated by `nuproducts` are not background subtracted, we do the background subtraction by `lcmath` with the background light curves scaled by the ratio of the integrated effective exposures within the source and background regions. The contributions of the background are just 2% and 0.03% of the total count rate during the low and high states, respectively. For the timing ephemeris, high-precision measurements of the binary parameters measured by the Green Bank Telescope, the Arecibo Observatory, and Parkes Observatory (Archibald et al. 2009) are adopted; however, the orbital period derivatives are not considered for simplicity. The top (a1) and fourth (b1) panels of Figure 3 show the folded low- and high-state light curves by `efold` with the orbital phase zero defined as the inferior conjunction (i.e., the companion is between the pulsar and the observer). For the quiescent folded light curve, it can be well described by a sinusoidal function with a peak amplitude of about 30% of the average intensity (significance is $\sim 10\sigma$). With the minimum intensity occurring at an orbital phase ϕ of 0 and 1, and the maximum at $\phi = 0.5$, it is unambiguously in phase with the optical modulation (Thorstensen & Armstrong 2005) and the soft X-ray (0.3–8 keV) modulation measured by *Chandra* (Bogdanov et al. 2011). We split the *NuSTAR* data into soft (3–10 keV) and hard (10–79 keV) energy band to search for an orbital-phase-dependent spectral variability that is absent in the *Chandra* data (Bogdanov et al. 2011). No statistically significant spectral variation has been found from the hard/soft ratio against orbital phase (Figure 3) that confirms the previous *Chandra* result.

For the high-state folded light curve, although a high variability is recorded with an extreme χ^2 value of $\sim$600 (dof = 15), the curve is not compatible with a sinusoidal function and is seemingly nonperiodic, indicating that the variability at this frequency is likely caused by random fluctuations instead of a combination of periodic signals. Interestingly, we tried to fold it with an arbitrary period, but the high variability is still present, strongly suggesting that the variability is likely to be dominated by other factors instead of the viewing angle at different phases. We note that soft X-ray rapid flickering is also seen by *Swift* during the X-ray high state (Patruno et al. 2014). We also performed a Lomb–Scargle analysis on the high-state data to search for other periodicity. After removing visually detected flaring states (timescales of the flares $\approx$100–1000 s) as well as some individual flares for which the count rate is higher than 3 counts s^{-1} in a 10 s bin (see the first panel of Figure 4 for details), a strong peak with a normalized power of $\sim 60\,\sigma^2_{\rm rms}$ is clearly seen in the periodogram at $f = (3.195 \pm 0.002) \times 10^{-4}$ Hz (equivalent to a period of $P = 3130 \pm 2$ s) in which the uncertainty is estimated by a bootstrapping technique with 5000 trials. The periodicity has not been detected by *Swift*/XRT during the earlier target-of-opportunity observations (Takata et al. 2014), probably due to the limited data quality of *Swift*, as the XRT data are fragmented into observations with several different short exposures. A similar analysis is also performed

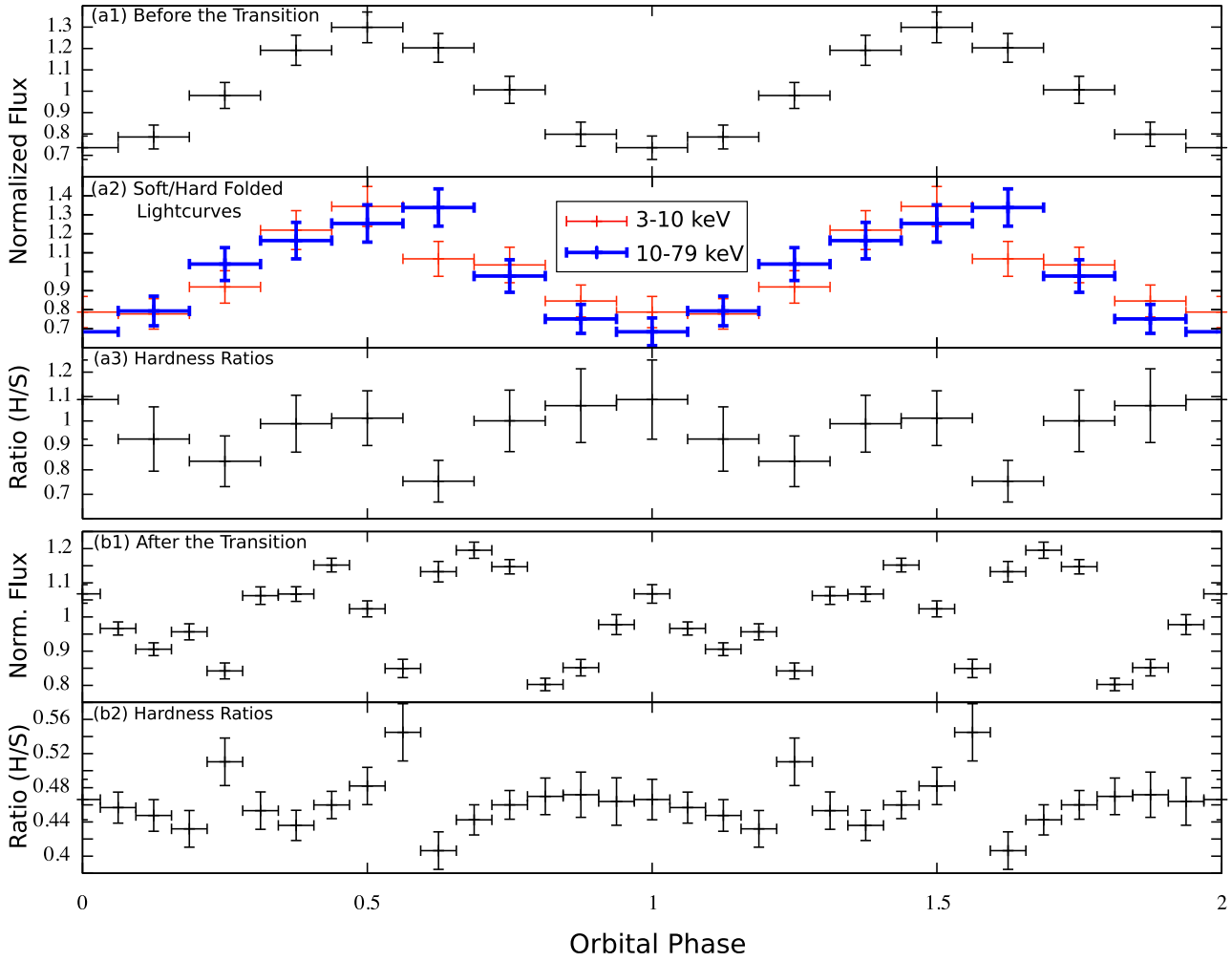

Figure 3. Barycentered *NuSTAR* light curves folded at the binary period ($P_{\rm orb}$ = 17115.512 s) with phase zero defined as the inferior conjunction. Top panel: full-band (3–79 keV) light curves during the rotation-powered state. Second panel: hard (blue/thick; 10–79 keV) and soft (red/thin; 3–10 keV) band light curves. Third panel: ratios between hard and soft band data points. Fourth panel: full-band (3–79 keV) light curves during the LMXB state. Fifth panel: ratios between hard and soft band data points.

(A color version of this figure is available in the online journal.)

on the *NuSTAR* low-state data as a control to test whether the periodicity is an intrinsic property of the pulsar binary or an instrumental pattern. Except three peaks corresponding to the orbital modulation of *NuSTAR* and its harmonic frequencies, the low-state periodogram is basically featureless, suggesting that the 3130 s periodicity is not systematic. Moreover, a light curve folded at the 3130 s period produces a quasi-sinusoidal modulation that is unlikely to be produced randomly (Figure 4). Indeed, the same modulation can also be produced by the soft and hard band data without any significant spectral variation. Besides the 3130 s periodicity, the power of the periodogram is significantly higher than the control one (i.e., up to 30 $\sigma^2_{\rm rms}$) around the frequencies from 10^{-4} to 3×10^{-3} Hz, implying variabilities with timescales ranging from a few minutes to a few hours are strong during the LMXB state. Short-term peculiar dips with variable lengths of 200–800 s are detected, which confirms the previous *Swift*/XRT finding of the low flux intervals ranging from 200 to 550 s (Takata et al. 2014).

4. DISCUSSION

We have found hard X-ray (3–79 keV) emission from the MSP/LMXB J1023 using *NuSTAR*. The hard X-rays were seen in both rotation-powered and LMXB states. At the distance of 1.3 kpc, the 3–79 keV luminosity is 5.8×10^{32} erg s^{-1} and 5.4×10^{33} erg s^{-1} during the rotation-powered state and the LMXB state, respectively. It is therefore not surprising that *Swift*/BAT could not detect J1023 (Stappers et al. 2014) because the sensitivity limit is at least two orders of magnitude higher. Compared to previous soft X-ray observations, the *NuSTAR* spectra are essentially the non-thermal extension from the soft X-rays. In both states, the broadband spectrum up to 79 keV can be fit with a simple power law with $\Gamma = 1.20$ ($\Gamma = 1.63$) in the low (high) state, which is more or less the same as the spectral shape derived from soft X-ray observations (Archibald et al. 2010; Bogdanov et al. 2011; Patruno et al. 2014; Takata et al. 2014). It is worth noting that a broken power-law model with a cutoff energy of 1.8 keV (Tam et al. 2010) or a thermal emission component from the neutron star (Bogdanov et al. 2011) can also describe the spectral shape during the rotation-powered state. However, *NuSTAR* is not sensitive to these soft X-ray features.

In terms of timing behavior, we found that the hard X-rays show the 4.8 hr orbital modulation during the low state, while it disappears in the high state (Figure 3). We will explain the X-ray orbital modulation using our model in this section later.

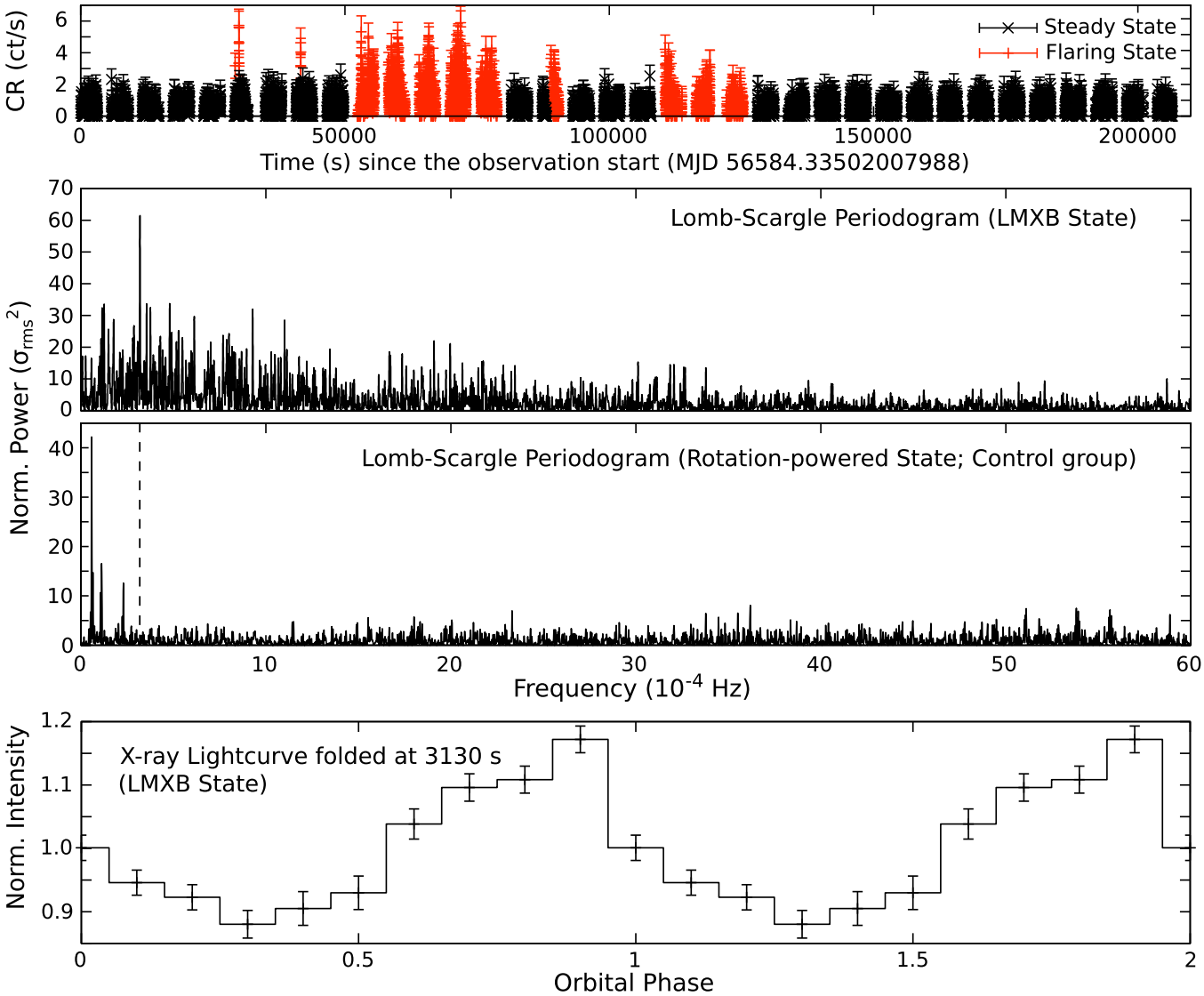

Figure 4. First panel shows the *NuSTAR* high-state light curve of J1023 with a binning factor of 10 s. Data in red indicate the flaring states while the black ones indicate the steady states that are used for the Lomb–Scargle analysis. The Lomb–Scargle periodogram of the high-state data is shown in the second panel with a control group of low-state data in the third panel of which the three highest peaks correspond to the orbital modulation and its harmonic frequencies. A peak of normalized power $\sim 60\sigma_{\rm rms}^2$ (false-alarm probability of the null hypothesis $\approx 10^{-23}$) at a frequency of $f = (3.195 \pm 0.002) \times 10^{-4}$ Hz (i.e., $P = 3130 \pm 2$ s) is clearly seen in the high state but is invisible during the low state (indicated by a dashed line), suggesting that it is not systematic. The last plot is the high-state light curve folded at 3130 s (with an arbitrary phase zero) indicating a quasi-sinusoidal brightness variation.

(A color version of this figure is available in the online journal.)

Moreover, short-term variabilities on timescales of 100–1000 s are seen in the high state, which are consistent with previous soft X-ray observations (Patruno et al. 2014; Takata et al. 2014). We speculate with our intrabinary shock model (Takata et al. 2014) that the observed variability is caused by either perturbation of shock front due to clumpy stellar wind or wind speed variation or sound propagation in the shock front. Similar short-term variability has also been found in two other known transitional MSP/LMXB systems, XSS J12270−4859 (de Martino et al. 2013) and IGR J18245−2452 (Ferrigno et al. 2014; Linares et al. 2014), during their X-ray high states. Such a short-timescale X-ray variability could be a common signature of MSP/LMXB systems in the LMXB state. Interestingly, a periodic modulation of 3130 s is found (see Figure 4), although its nature is not clear. Additional X-ray observations during the LMXB state are required to better determine the origin.

In the soft X-ray band, the high-energy emission in general is explained by thermal emission from the neutron star surface and non-thermal emission produced in pulsar magnetospheres. Furthermore, X-ray emission in form of X-ray nebulae can be powered by MSPs, while intrabinary shock within the binary system can also generate X-rays when the pulsar wind interacts with the materials from the companion star (e.g., Kong et al. 2012; Takata et al. 2014; Hui et al. 2014). It is also suggested that accretion onto the neutron star magnetosphere can produce the non-thermal X-rays (Campana et al. 1998). More recently, it has been proposed that the state transition of another transitional MSP/LMXB IGR J18245−2452 is due to transition between magnetospheric accretion and intrabinary shock emission (Linares et al. 2014) or a propeller effect (Papitto et al. 2013). Propeller effect was also suggested to explain the state transition of J1023 (Archibald et al. 2009; Patruno et al. 2014).

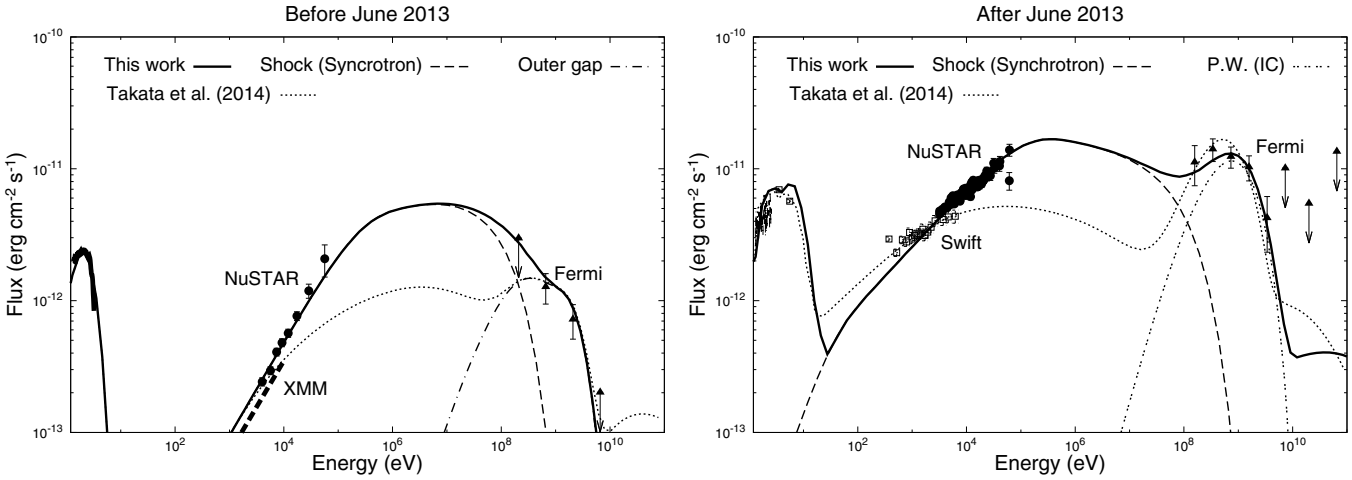

Figure 5. Multi-wavelength spectra before (left) and after (right) 2013 June. The solid lines and dotted lines represent the calculated spectra in this work and in Takata et al. (2014), respectively. The dashed–dotted line in the left panel shows the spectrum of the outer gap emissions, and the double-dotted line in right panel shows the inverse-Compton spectrum of the cold-relativistic pulsar wind. For shock emissions (dashed lines), we assume the shock is located at $r_s = 3 \times 10^{10}$ cm and assume that 10% and 70% of the pulsar wind is stopped by the shock before and after 2013 June, respectively. In addition, the power-law indexes of the shocked particles are assumed to be $p = 1.5$ and $p = 2$ before and after 2013 June, respectively. A more detailed calculation method is given in Takata et al. (2014).

In Takata et al. (2014), we propose a theoretical model to explain the multi-wavelength (from UV to GeV gamma-ray) observations of J1023. For the low state (before 2013 June), we assumed that the momentum ratio between the stellar wind and the pulsar wind, $\eta = \dot{M} v_w c / L_{\rm sd}$, is much smaller than unity, that is, $\eta = 0.3(\dot{M}/5 \times 10^{15}\,{\rm g\,s^{-1}})(v_w/10^8\,{\rm cm\,s^{-1}})(L_{\rm sd}/5 \times 10^{34}\,{\rm erg\,s^{-1}})^{-1}$, and therefore the shock in low-state phase (i.e., radio pulsar phase) is close to the L1-Lagrangian point. The size of the emission region was approximately described by the size of the Roche lobe. In such a case, the observed X-ray modulation in the low state will be caused by the eclipse of the emission region (see Bogdanov et al. 2011). However, we found in Figure 5 that the predicted flux above 10 keV in Takata et al. (2014) is about one order of magnitude smaller than that measured by the *NuSTAR*. Furthermore, Archibald et al. (2013) argued that it is not clear how such a shock geometry, which surrounds the companion, can explain the length (~0.6 orbital phase centered at the inferior conjunction) of the observed 350 MHz eclipse, and therefore the shock should cover the pulsar. This would indicate that the system is dominated by the outflow from the companion star and the mass-loss rate is larger than $\sim 2 \times 10^{16}\,{\rm g\,s^{-1}}$. Archibald et al. (2013) argued that the large mass-loss rate would be incompatible with the dispersion measure, and therefore they suggested that the magnetic pressure of the companion star is against the pulsar wind. For example, we may assume the stellar magnetic field is $B(R) = B_*(R_*/R)^2$ (see Archibald et al. 2013 and references therein), where R is the distance from the center of the companion and B_* is the magnetic field at the surface. In addition, the radius of the companion star (R_*) is estimated as the Roche lobe radius, $R_* \sim 0.462[q/(1+q)]^{1/3} a \sim 3 \times 10^{10}$ cm with $q = 0.2\,M_\odot/1.4\,M_\odot \sim 0.14$ being the mass ratio and $a \sim 1.3 \times 10^{11}$ cm the separation between the two stars. The distance to the apex of the shock from the pulsar will be estimated from $r_s/a \sim 1/(1+\eta_b^{1/2})$, where $\eta_b = B_*^2 R_*^2 c / L_{\rm sd} \sim 5(B_*/10^2\,{\rm G})^2(R_*/2\times10^{10}\,{\rm cm})^2(L_{\rm sd}/5\times10^{34}\,{\rm erg\,s^{-1}})^{-1}$. Hence, the shock could wrap the pulsar if the magnetic field at the stellar surface is larger than $B_* \sim 10^2$ G. In the present calculation, we use $\eta_b \sim 7$, which corresponds to the shock radius $r_s \sim 3 \times 10^{10}$ cm, to fit the X-ray data with the emission model.

Figure 5 shows the results of our revised model fitting for the multi-wavelength observations including the *NuSTAR* data. In the present calculation, the fraction of the pulsar wind stopped at the shock apex $r \sim r_s$, and the magnetization parameters are used as the free parameters. To fit the X-ray observations of the low state (left panel), we assumed that about 10% of the pulsar wind is stopped at around the shock apex $r \sim r_s$, and we also assumed a magnetization parameter of $\sigma \sim 10^{-2}$ at the shock. To explain the hard spectrum of the X-ray emissions, we assume $p = 1.5$ as the power index of the accelerated particles at the shock. The predicted luminosity of the emissions from the pulsar (outer gap model) and pulsar wind (shock) is $L_{\rm gap} \sim 5\times10^{33}\,{\rm erg\,s^{-1}}$ and $L_{\rm pw} \sim 4\times10^{33}\,{\rm erg\,s^{-1}}$, respectively. We note that the *observed* GeV luminosity ($\sim 5 \times 10^{32}\,{\rm erg\,s^{-1}}$) in low state is smaller than the predicted luminosity of the outer gap model. We expect that our line of sight cuts through the edge of the gamma-ray beam and the apparent luminosity is smaller than the intrinsic luminosity.

In the present model, the shock is located in the pulsar side and the observed orbital modulation of the X-ray emissions is explained by Doppler boosting due to the finite velocity of the shocked pulsar wind. The Doppler boosting introduces an orbital modulation of the emissions that are isotropic in the co-moving frame with the flow. Figure 6 compares the model light curve and the *NuSTAR* observation. For the model, we assume $v = 0.4c$ for the velocity of the shocked pulsar wind to explain the observed amplitude.

The UV/optical emissions of the high state (after 2013 June) come from the accretion disk and are also responsible for generating additional GeV gamma-rays via inverse-Compton scattering of the cold-relativistic pulsar wind. In this model, we expect that the accretion disk in the high state does not come into the pulsar magnetosphere, and the rotation-powered activities of the pulsar are still turned on. For a standard disk model (Frank et al. 2002), the gas pressure of the disk at the distance r from the pulsar is

$$P_{\rm disk}(r) \sim 3.6\times10^4 \mu^{-1}\alpha^{-9/10}\dot{M}_{16}^{17/20} M_1 r_{10}^{-21/8}\,{\rm dyn\,cm^{-2}}, \quad (1)$$

where μ is the average molecular weight, α is the viscosity parameter, $\dot{M}_{16}$ is the mass-loss rate of the companion

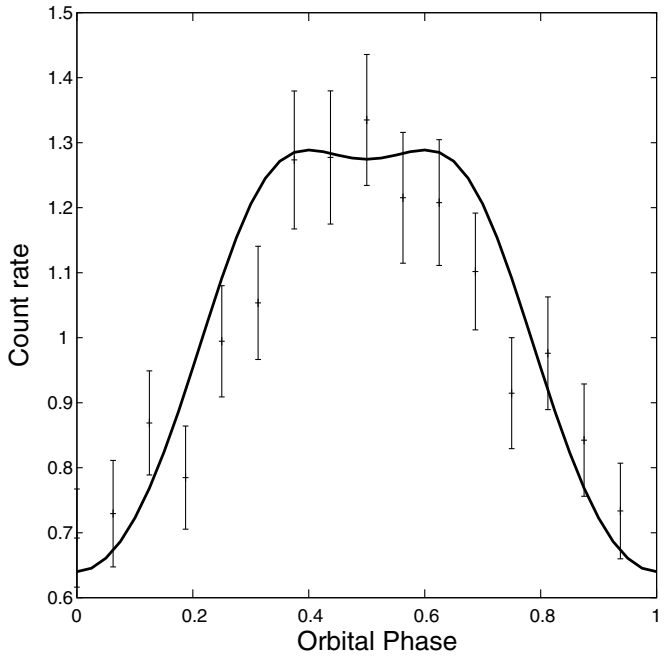

Figure 6. Orbital modulation of the X-ray emissions before 2013 June. Phase zero corresponds to the inferior conjunction, where the companion is located between the pulsar and Earth. In the present model, the Doppler boosting causes the orbital modulation. The solid line shows the model light curve with shock geometry characterized by the momentum ratio $\eta = 7$ and the velocity $v \sim 0.4c$ of the shocked pulsar wind.

in units of $10^{16}\,\mathrm{g\,s^{-1}}$, M_1 the neutron star mass in units of the solar mass, and $r_{10} = (r/10^{10}\,\mathrm{cm})$. One finds that this gas pressure dominates the pulsar wind pressure, $P_{\rm PW} \sim L_{\rm sd}/4\pi r^2 c \sim 1.3\times10^3 (L_{\rm sd}/5\times10^{34}\,\mathrm{erg\,s^{-1}}) r_{10}^{-2}\,\mathrm{dyn\,cm^{-2}}$, below L1-Lagrangian point ($r_{L1} \sim 8\times10^{10}\,\mathrm{cm}$ from the pulsar), and the pulsar wind cannot stop the migration of the accretion disk. Takata et al (2010, 2012), however, argued that the gamma-rays from the pulsar magnetosphere irradiating the accretion disk are absorbed by the disk matter through a pair-creation process in the presence of a nucleus (Liang 1999), and the energy transfer from the gamma-rays to the disk matters causes an evaporation of the disk. Applying a standard disk model (Frank et al. 2002), we found that the disk column density below $r \sim 3\times10^9$ cm from the pulsar is high enough to absorb the gamma-rays. In this model, the evaporation rate from the disk is calculated from $\zeta L_{\rm sd} = \dot{M}_{\rm ev} v_{\rm es}^2/2$ with ζ being irradiation efficiency and $v_{\rm es}$ escape velocity, and it is estimated as $\dot{M}_{\rm ev} \sim 2\times10^{16}(\zeta/0.01)(r/3\times10^9\,\mathrm{cm})(L_{\rm sd}/5\times10^{34}\,\mathrm{erg\,s^{-1}})\,\mathrm{g\,s^{-1}}$; that is, if the efficiency is $\zeta \sim 1\%$ (about 10% of the gamma-ray luminosity), most of the disk matter from the companion star will be evaporated at $r \sim 3\times10^9$cm, and the disk will be outside the light cylinder, indicating the rotation-powered activities of the pulsars are still on in the high state. In our model, the X-ray emissions are produced by the intrabinary shock due to the interaction of the pulsar wind with the outflow from the star/disk.

For the high state (since 2013 June), we found that the X-ray emissions do not show the orbital modulation (Section 3.2). This would suggest that the shock enshrouds the pulsar and stops almost all of the pulsar wind. Since the pulsar is surrounded by the disk, it would be possible that the outflow matter from the disk caused by the irradiation of intense pulsar wind/high-energy radiation stops most of the pulsar wind. In the present model, the momentum ratio of outflow matter from the disk and the pulsar wind may be estimated from $\eta \sim \dot{M}_{\rm ev} v_{\rm es} c/L_{\rm sd} \sim 2(\dot{M}_{\rm ev}/10^{16}\,\mathrm{g\,s^{-1}})(v_{\rm es}/3\times10^8\,\mathrm{cm^{-1}})(L_{\rm sd}/5\times10^{34}\,\mathrm{erg\,s^{-1}})^{-1}$, suggesting the shock enshrouds the pulsar. Because we do not know the exact geometry of the shock, which may be more complicated than a spherical shape, we assume that the shock distance from the pulsar does not depend on the direction. In our calculation, we assumed the shock distance $r_s \sim 3\times10^{10}$ cm and the magnetization parameter at the shock $\sigma \sim 10^{-2}$ are the same as the shock parameters of the low state. To explain the increase of the observed flux since 2013 June, we assumed that ~70% of the pulsar wind is stopped by the shock. We also used power index $p = 2$ of the particle distribution to explain the hardness of the X-ray spectrum. The right panel of Figure 5 compares the model calculation with the multi-wavelength observations for the high state. The GeV gamma-ray emission in the high state is explained by the inverse-Compton process between the pulsar wind and UV/optical emissions from the disk. The calculated total luminosity from the pulsar wind is $L_{\rm pw} \sim 3\times10^{34}\,\mathrm{erg\,s^{-1}}$.

The *NuSTAR* data of J1023 provide the first hard X-ray spectra extending to 79 keV for a transitional MSP/LMXB in both the MSP and LMXB states. Together with multi-wavelength observations from radio to gamma-ray, these high-quality *NuSTAR* spectra allow us to constrain the high-energy emission mechanisms, and we show that the data above 10 keV are crucial. In summary, the length of 350 MHz eclipse in the low state may suggest that the outflow from the companion star dominates the pulsar wind and the shock surrounds the pulsar. This could be due to a large mass-loss rate $\dot{M} > 2\times10^{16}\,\mathrm{g\,s^{-1}}$ of the stellar wind or of the existing magnetic pressures of the star. In such a geometry, the orbital modulation of the X-rays is caused by Doppler boosting due to the finite velocity of the shocked pulsar wind. The disappearance of the orbital modulation of the X-rays founded by *NuSTAR* during the LMXB state may indicate that the evaporating matter from the disk due to the pulsar irradiation stops almost all the pulsar wind.

We note that at the time of revising this paper, a paper by the *NuSTAR* team using the same data sets has been recently accepted for publication (Tendulkar et al. 2014) and their results are entirely consistent with ours.

K.L.L., A.K.H.K., and R.J. are supported by the Ministry of Science and Technology of the Republic of China (Taiwan) through grants 100-2628-M-007-002-MY3, 100-2923-M-007-001-MY3, and 101-2119-M-008-007-MY3. J.T. and K.S.C. are supported by a GRF grant of the HK Government under HKU 17300814P. P.H.T. is supported by the Ministry of Science and Technology of the Republic of China (Taiwan) through grant 101-2112-M-007-022-MY3. C.Y.H. is supported by the National Research Foundation of Korea through grant 2011-0023383. This research has made use of the *NuSTAR* Data Analysis Software (NuSTARDAS) jointly developed by the ASI Science Data Center (ASDC, Italy) and Caltech (USA).

Facilities: NuSTAR, *Swift*

REFERENCES

Alexander, D. M., Stern, D., Del Moro, A., et al. 2013, ApJ, 773, 125
Alpar, M. A., Cheng, A. F., Ruderman, M. A., & Shaham, J. 1982, Natur, 300, 728
Archibald, A. M., Kaspi, V. M., Bogdanov, S., et al. 2010, ApJ, 722, 88
Archibald, A. M., Kaspi, V. M., Hessels, J. W. T., et al. 2013, ApJ, submitted (arXiv:1311.5161)
Archibald, A. M., Stairs, I. H., Ransom, S. M., et al. 2009, Sci, 324, 1411
Bassa, C. G., Patruno, A., Hessels, J. W. T., et al. 2014, MNRAS, 441, 1825
Bogdanov, S., Archibald, A. M., Hessels, J. W. T., et al. 2011, ApJ, 742, 97

Bond, H. E., White, R. L., Becker, R. H., & O'Brien, M. S. 2002, PASP, 114, 1359
Campana, S., Colpi, M., Mereghetti, S., Stella, L., & Tavani, M. 1998, A&ARv, 8, 279
de Martino, D., Belloni, T., Falanga, M., et al. 2013, A&A, 550, A89
Ferrigno, C., Bozzo, E., Papitto, A., et al. 2014, A&A, 567, A77
Frank, J., King, A., & Raine, D. 2002, Accretion Power in Astrophysics (Cambridge: Cambridge Univ. Press),
Harrison, F. A., Craig, W. W., Christensen, F. E., et al. 2013, ApJ, 770, 103
Homer, L., Szkody, P., Chen, B., et al. 2006, AJ, 131, 562
Hui, C. Y., Tam, P. H. T., Takata, J., et al. 2014, ApJL, 781, L21
Kong, A. K. H. 2013, ATel, 5515, 1
Kong, S. W., Cheng, K. S., & Huang, Y. F. 2012, ApJ, 753, 127
Liang, E. 1999, A&AS, 138, 529
Linares, M., Bahramian, A., Heinke, C., et al. 2014, MNRAS, 438, 251
Papitto, A., Ferrigno, C., Bozzo, E., et al. 2013, Natur, 501, 517
Patruno, A., Archibald, A. M., Hessels, J. W. T., et al. 2014, ApJL, 781, L3
Romanova, M. M., Ustyugova, G. V., Koldoba, A. V., & Lovelace, R. V. E. 2009, MNRAS, 399, 1802
Stappers, B. W., Archibald, A. M., Hessels, J. W. T., et al. 2014, ApJ, 790, 39
Takata, J., Cheng, K. S., & Taam, R. E. 2010, ApJL, 723, L68
Takata, J., Cheng, K. S., & Taam, R. E. 2012, ApJ, 745, 100
Takata, J., Li, K. L., Leung, G. C. K., et al. 2014, ApJ, 785, 131
Tam, P. H. T., Hui, C. Y., Huang, R. H. H., et al. 2010, ApJL, 724, L207
Tendulkar, S. P., Yang, C., An, H., et al. 2014, ApJ, 791, 77
Thorstensen, J. R., & Armstrong, E. 2005, AJ, 130, 759
Wang, Z., Archibald, A. M., Thorstensen, J. R., et al. 2009, ApJ, 703, 2017
Wijnands, R., & van der Klis, M. 1998, Natur, 394, 344